Zirconium hydride precipitation kinetics in Zircaloy-4 observed with synchrotron X-ray diffraction

M.S. Blackmur [a,*], J.D. Robson [a], M. Preuss [a], O. Zanellato [b], R.J. Cernik [a], S.-Q. Shi [c], F. Ribeiro [d], J. Andrieux [e]

[a] Materials Performance Centre, School of Materials, The University of Manchester, Manchester M1 7HS, United Kingdom
[b] PIMM, Ensam – Cnam – CNRS, 151 Boulevard de l'Hôpital, 75013 Paris, France
[c] Department of Mechanical Engineering, The Hong Kong Polytechnic University, Hung Hom, Kowloon, Hong Kong, China
[d] Institut de Radioprotection et de Sûreté Nucléaire, CEN Cadarache, 13115 St. Paul Les Durance, France
[e] Beamline ID15, European Synchrotron Radiation Facility, Grenoble, France

ABSTRACT

High-energy synchrotron X-ray diffraction was used to investigate the isothermal precipitation of δ-hydride platelets in Zircaloy-4 at a range of temperatures relevant to reactor conditions, during both normal operation and thermal transients. From an examination of the rate kinetics of the precipitation process, precipitation slows with increasing temperature above 200 °C, due to a reduction in the thermodynamic driving force. A model for nucleation rate as a function of temperature was developed, to interpret the precipitation rates seen experimentally. While the strain energy associated with the misfit between hydrides and the matrix makes a significant contribution to the energy barrier for nucleation, a larger contribution arises from the interfacial energy. Diffusion distance calculations show that hydrogen is highly mobile in the considered thermal range and on the scale of inter-hydride spacing and it is not expected to be significantly rate limiting on the precipitation process that takes place under reactor operating conditions.

1. Introduction

1.1. Zirconium and zirconium alloys

Zirconium alloys have been widely adopted as cladding material for fuel rods in Western light water reactors (LWRs) ever since nuclear reactor technology was first conceived at the end of the 1940s [1]. The function of this cladding is to act as a structural component, containing fuel pellets, holding them in place within a fuel assembly and allowing the desired turbulent flow of coolant between rods, while conducting heat energy from the fuel into the fluid [2]. Additionally, it also acts as a buffer between the fuel pellets and the encompassing reactor environment by containing fission products that escape the fuel, whilst preventing degradation of the fuel from exposure to the coolant medium [2–4]. This means that the structural stability of these components is of paramount importance, as it is linked intrinsically to the safety, efficiency and operability of the fuel assembly [2]. The choice of available materials is limited, as fuel assembly components are expected to last years under typical operating conditions – where temperatures range from 280 °C to 400 °C and coolant pressures are in excess of 15 MPa – as well as performing adequately during potential accident scenarios, where conditions are significantly more harsh [2,5,6].

The selection of zirconium alloys as cladding stems from the advantageous mechanical properties, good corrosion behaviour and, critically, the low neutron absorption cross-section that they demonstrate [1,4,7]. However, the common commercially deployed alloys of zirconium display a high affinity for both oxygen and hydrogen [8,9]. When exposed to the light water coolant, some of the hydrogen by-product of the oxidation reaction is absorbed into the cladding, though the mechanism for this ingress through the oxide is still debated [10]. While the solubility limit of oxygen in α-zirconium is as high as 28.5 at.% under typical light water reactor operating conditions [11], the hydrogen solubility in the same environment is at most 3 at.% [12]. Once the local hydrogen concentration exceeds the terminal solid solubility of the alloy for the local temperature, any excess will then precipitate into hydride phase. Given the general tendency for hydrogen to diffuse down thermal and concentration gradients, and up hydrostatic stress gradients, macroscopic hydrogen distribution can often be non-uniform within components [13]. This is further compounded in fuel cladding, where the coolant removes heat

from the outer surface of the material, while the fuel itself heats the inner surface. Together, these mechanisms lead to dramatic differences in concentration and solubility between different regions, leading to phenomena like the formation of hydride rims [14].

1.2. Zirconium hydrides

Since the early days of nuclear technology, researchers have investigated the impact of hydrogen on zirconium alloys, as well as various aspects of the formation and properties of hydrides [15–21]. When precipitating, hydrides take the morphology of either needles or platelets, based on the cooling rate and the availability of hydrogen [21]. These variables influence which of the hydride phases precipitate, where the most commonly observed form is the non-stoichiometric face-centred cubic delta (δ) phase [22]. Less commonly, the stable/metastable (based on temperature and interpretation [23]) gamma (γ) or stable epsilon (ε) hydrides, both taking a face centred tetragonal crystal structure, may also precipitate [23].

The physical shape that each of these different phases take, on a fine scale and in isolation, is primarily ascribed to the anisotropic directionality of the stress-free transformation strains of each, generated during phase change [15]. This misfit is the product of an increase in volume that occurs in newly developed hydrides due to their lower density, when compared to that of the parent matrix [24]. In the case of δ-hydride, where the face-centered cubic unit cell is isotropic in the three principle axes, the anisotropy of the hexagonal close packed cell of the parent α-zirconium matrix leads to similar anisotropy in the transformation strain [15]. When δ precipitates, the misfit normal to the basal plane is calculated by Carpenter to be 7.2%, while that normal to the prismatic plane is only 4.58% [15]. This encourages isotropic growth in the basal plane while retarding that in the prismatic plane, potentially yielding a 'micro'-hydride with a platelet type morphology. These precipitates will be oriented with platelet normals parallel to the matrix hexagonal unit cell basal normal. More recently, Barrow measured transformation strains of 5.5%, 3.1% and 0.5% in the $[0001]_\alpha$, $[11\bar{2}0]_\alpha$ and $[\bar{1}100]_\alpha$ directions, respectively [25]. Interestingly, these values imply that δ-hydrides would not precipitate with the commonly described platelet morphology, and are instead described as needle-like structures by the author [25].

During their evolution, micro-hydride precipitates have a tendency to group or stack with discrete separating distances to form the comparatively large hydride features often observed through optical microscopy [21,26–28]. This chaining effect is attributed to the development of a hydrogen atmosphere at the core of dislocations generated locally by hydride precipitation, as encouraged by the resulting lattice dilation in these defects [29]. The morphology, distribution and orientation of these 'macro'-hydrides are produced as a function of the thermal history, residual and applied stresses, texture, and microstructure of a component [24].

For example, where there are high cooling rates or large matrix grains, a predominance of intra-granular hydrides are observed, while lower cooling rates or small grain sizes produce more inter-granular or grain boundary hydrides [21,28,30]. Similarly, macro-hydride orientation is heavily influenced by applied stresses, where compressive forces reorient hydrides with their normal perpendicular to the loading direction [21]. An applied tensile load, however, will align macro-hydrides with their normal parallel to the loading direction [15,21].

This macroscopic reorientation of hydrides is actually a process wherein the existing micro-hydrides within a macro-precipitate will dissolve and re-precipitate with a new macro-distribution, possessing an apparent normal parallel with the tensile component of an applied three-dimensional stress. In practice, the thermomechanical history of the alloy will control the natural orientations of macro-hydrides precipitated in a component with no load [31]. However, should a fuel rod be exposed to an applied stress above a certain threshold, the reorientation phenomena occurs, where the threshold value is determined by processing and microstructure [31]. Despite differences in macro-morphology and orientation, all micro-hydrides are found to possess the same orientation relationship relative to the matrix of $(0001)_\alpha \| (111)_\delta$ [24,28,30], irrespective of reorientation; although there are some examples of $\{10\bar{1}7\}_\alpha \| \{111\}_\delta$ found in radially oriented inter-granular hydrides [32]. Phase field and finite element models have gone on to simulate and explain this orientation relationship in works like [33,34].

Hydrides, once precipitated in zirconium, degrade the mechanical properties of a component, leading to reductions in tensile strength, ductility and fracture toughness [35–40]. These changes can ultimately compromise the integrity of cladding during normal operating life , accident conditions and fuel storage [13]. As well as the degradation of mechanical properties, the presence of hydrides can also affect phenomena like pellet cladding mechanical interaction (PCMI); or introduce mechanisms for failure, such as delayed hydride cracking (DHC). The former mechanism is the product of thermal expansion in fuel pellets introducing stresses into the cladding, which may then lead to the formation of cracks in areas made brittle by large hydride concentrations [13]. The latter mechanism, DHC, is a sub-critical, time dependent cracking phenomenon that requires long range hydrogen diffusion for repeated local hydride growth and fracture at a hydrostatic tensile stress raiser [5,41,42]. The process occurs over an extended period of time under a continuously applied load that is below the yield stress of the material [5,41,42].

Experimental techniques employed to investigate the general morphology and distribution of hydrides during precipitation/dissolution, as well as during the related mechanisms of failure, are limited because microscopy can only provide information for a single point in time. Moreover, investigating components that have been irradiated during service life is both costly and difficult, making evaluations of real end of life microstructures problematic [43]. Synchrotron X-ray diffraction, on the other hand, provides an excellent tool for studying bulk processes taking place within materials, giving the ability to sample relatively large volumes of material while performing in-situ experiments [27]. The propensity of a synchrotron to produce a highly collimated, high-flux beam yields a significant degree of angular resolution, allows for rapid diffraction pattern acquisition, and generates very well defined peaks with minimal artificial broadening. This is especially valuable when studying the precipitation process that takes place when hydrogen saturates zirconium, as measurements of very weak reflections, that may otherwise be overlapped by dominant zirconium peaks, can be made during thermal [23,27,44] or mechanical [22,24,31] experiments.

In tandem with the experimental work undertaken to study the zirconium-hydrogen system, modelling has also been performed to understand better the precise mechanisms involved in the nucleation, growth, mechanical properties of these precipitates and their effect on zirconium cladding. Following on from the work undertaken by Carpenter to define the stress-free transformation strains in δ- and γ-hydrides, Singh et al. were able to extend the methodology to describe volumetric misfit as a function of temperature [15,45]. This work serves to illustrate the temperature dependence of the misfit in the hydride system, where an additional $\approx$11% misfit arises from a 275 °C increase in temperature, demonstrating the significant impact of thermal changes on hydride properties [45].

Barrow et al., in their evaluation of the impact of chemical and strain energy on hydride nucleation, model both the chemical driving force and strain energy associated with hydride nucleation, as a function of terminal solid solubility on precipitation, or TSSP, temperature (and thus bulk hydrogen content) [46]. From a comparison of the magnitude of these values, this work demonstrates the dominance of the chemical free energy contribution to driving force as the primary factor influencing the nucleation of hydrides [46]. Further to this, it is stated that the energy barrier to nucleation is dominated by the surface (or interfacial) energy, as opposed to strain energy, given that large elastic strains tend to be plastically relaxed through the formation of dislocations [46].

Interestingly, in other work, Barrow puts forward a precipitation process where γ-hydride nucleates and grows, before transforming into δ-hydride, yielding a precipitate with a core consisting of δ- and tips of γ-hydride [25]. Given that the γ-hydride has a lower accommodation energy than the δ-phase, it may be physically reasonable to suppose it acts as a precursor, before transforming during the process of coarsening [25]. If δ were considered the stable phase and γ metastable, this would imply there was some other factor preventing the stable phase from forming initially. Another interpretation states that the γ-phase is stable and δ metastable, which would account for the initial formation of γ, the transformation to δ would then be the product of a destabilisation of γ, in favour of δ.

More recently, advances in phase-field modelling have allowed for the simulation of hydride precipitation with defined time and length scales, both with and without applied load [43,47,48]. The evolution of elastic stresses within the surrounding matrix can then be predicted for a range of hydride distributions, and the work presented in [48] shows a good agreement between simulated morphologies and those seen experimentally. While these simulations have only been performed on γ-hydride thus far, the methodology employed can easily be extended to model δ-precipitates. The phase-field methodology has also been used to demonstrate the effect of uniaxially applied load on hydride precipitation, where precipitates whose normals are aligned close to the tensile force are those predicted to show the most growth [49].

This work, stemming from a set of kinetic synchrotron X-ray diffraction experiments, seeks to quantify the rapid isothermal precipitation that takes place where significant undercooling is in effect. To support these observations, a simple model describing nucleation rate as a function of the experimental temperatures is described. This model and associated calculations are designed to build upon the work of other authors whom have produced expressions that describe the chemical, strain and interfacial energies of either a misfitting precipitate or the hydride system itself [50–52].

2. Experimental

2.1. Sample specification

A single specimen of Zircaloy-4 measuring 50 mm × 5 mm × 0.4 mm was used in this work, which was provided by the Institut de Radioprotection et de Sûreté Nucléaire, France. As with the work presented by Zanellato et al., the material was rolled to 400 μm and recrystallised, yielding an average grain diameter of 10 μm and the strong basal texture associated with recrystallisation within rolled plate with a hexagonal close packed crystal structure [27]. The Kearns factors (details in [53]) for this material, as calculated from EBSD analysis, were f_{RD} = 0.107, f_{TD} = 0.219 and f_{ND} = 0.673. Following thermo-mechanical processing, the sample was charged with hydrogen to a specified average concentration using the methodology for charging and verification described by Zanellato et al. [27]. Hot extraction was used to verify the

concentration, and the result of charging was found to be within ±15 ppm$_{wt.}$ of the desired content, with gradients across the sample of 3 ppm$_{wt.}$ mm^{-1} on average [27]. At the time of the experiment, the hydrogen concentration within the sample was measured to be approximately 430 ppm$_{wt.}$, corresponding to the approximate hydrogen content of cladding material that has had a burnup of 49 GWd/t$_U$; close that listed for current fuel assemblies [54,55].

2.2. Synchrotron X-ray diffraction parameters

The experimental work presented herein was carried out at the European Synchrotron Radiation Facility (France), on high energy beamline ID15B; a full technical description of the beamline can be found in [56,57]. Diffraction was undertaken using transmission geometry with the beam normal to the surface of the specimen, allowing for a large volume of material to be sampled through the thickness of the sheet. Debye–Scherrer rings were recorded using a Trixell Pixium 4700 detector. An acquisition time of 5 s and an average disk write time of 4–5 s was achieved, yielding a temporal resolution of 9–10 s per recorded diffraction pattern. Throughout this experiment a monochromatic beam with a consistent energy of E = 87.17 ± 0.01 keV, and corresponding wavelength of λ = 0.14223 Å, was used to illuminate the specimen, in conjunction with a beam geometry of 300 × 300 μm^2.

2.3. Thermal transients

The material was mounted in the water-cooled and electrically conductive grips of an Instron ElectroThermal Mechanical Tester (ETMT8800), which was used to drive the thermal cycles using resistive (or Joule) heating. As zirconium alloys display a strong tendency to oxidise at elevated temperatures, a slow flowing atmosphere of inert argon gas was supplied into the sealed and oxygen purged chamber in which the sample was mounted. The temperature of the sample was set and maintained by an automatic feedback loop, which measured the temperature of the sample using an S-Type thermocouple spot-welded to the axial centre of the sample, close to the location of the incident beam. The readings of the thermocouple were fed back to the control unit in order to adjust the heating current accordingly, to produce the desired temperature.

As a check of the thermocouple, Laboratory X-ray Diffraction (LXRD) was undertaken on the same sample, and a comparison of thermal expansion coefficients measured through SXRD and LXRD was made. This secondary check of thermal expansion is employed as flaws in the spot welding of the thermocouple used in the ETMT can lead to erroneous temperature readings [58]. Both techniques showed good agreement in measured thermal expansion, and so the thermocouple was deemed a reliable measure of temperature.

The thermal profile for the experiment was comprised of one ramped transient, followed by seven quench and dwell cycles. The initial cycle (C1), designed to measure solubility curves, heated at a rate of 1 °C s^{-1} from a base temperature (T_{floor}) of 40 °C up to a peak (T_{max}) of 570 °C, above the expected eutectoid temperature [59,60]. Holds were implemented in this cycle at T_{max} and at 300 °C as part of both heating and cooling ramps, during which lateral scans along the axial length of the sample were made to evaluate hydride distributions across the sample at elevated temperature. During cooling in this cycle, a rate of 1 °C s^{-1} was employed to mirror the heating operation.

The terminal dissolution solubility for the sample was measured from C1 to be 439 °C, which is lower than the 513 °C predicted by McMinn for this concentration, and so a T_{max} of 500 °C was set for all following transients [60]. Each of the subsequent

quench-based cycles (C2–C8) involved raising the temperature to T_{max} and holding for 15 min in order to fully dissolve all hydrides.

Given that a hydride precipitation memory effect has been discussed in the literature, [19,61], this process would impact on the precipitation solvus and kinetics recorded during all cycles. By dwelling at elevated temperatures for a period after all hydrides have been dissolved, some of the dislocations left behind by previous hydride structures or cold work were given the chance to recover. Along with this, residual stresses may also have been allowed to relax, the combination of which could reduce the possibility of heterogeneous nucleation at preferential sites, supporting an assumption of homogeneous nucleation throughout the experiment.

Following each dissolution hold, the sample was then 'quenched' by reducing the current used to heat the sample to achieve the desired dwell temperature for kinetics observations. In practice, heat loss through conduction into the grips and radiation into the surrounding atmosphere did not allow instantaneous quenching, and a maximum cooling rate of approximately $30\,°C\,s^{-1}$ was observed. In the case of the largest change in temperature seen in this experiment ($\Delta T = 400\,°C$), this would mean it took 13.3 s to reach the target temperature, however, observations were made from the onset of the cooling operation.

Following each quench, the temperature was held steady in the isothermal region that forms the basis of the analytical work presented, and from which all kinetics observations are made. Finally, the sample was cooled back to T_{floor}, where axial hydride distribution checks were made after each thermal cycle. The desired dwell temperatures started at 100 °C and rose by 50 °C in 7 cycles up to 400 °C. No measurable hydride peak was detected during the final 400 °C cycle, despite the hold temperature being below the TSSP predicted by McMinn (445 °C) [60]. From C1, the TSSP measured for the sample was found to be 361 °C, potentially explaining why no hydride signal was detected during C8 and indicating that only minimal precipitation would be expected during C7 at 350 °C. Additionally, a $1\,°C\,s^{-1}$ heating ramp was added at the beginning of the 350 °C cycle to investigate long term changes to solubility towards the end of the experimental run. Only a minimal change in the TSSD curve was observed, which was well within the expected experimental error of $\pm15.5\,ppm_{wt.}$. A schematic diagram, presented as Fig. 1, shows the thermal regime implemented throughout this experiment.

The hydrogen distribution checks made at T_{floor} between each cycle and at elevated temperatures during C1 were performed as resistive heating produces a thermal gradient across the axial

length of the material, emphasised by the loss of heat from the edges of the specimen due to water cooling in the grips [58]. This is particularly significant in this work as it is well documented that hydrogen has a strong tendency to diffuse towards cooler regions, potentially leading to hydrogen depletion in the significantly hotter axial centre of the sample, where measurements were taken [13,62,63]. The result of these checks confirmed that the thermal gradient did result in regions of marked depletion and enrichment, however, the most significant of these were primarily localised to material within 5 mm of the grips (the total length between grips being 20 mm). The central region, from where measurements were taken, showed only a gradual depletion of hydrogen available for precipitation, where the difference at the point of diffraction between the initial state and the final state was no more than $30\,ppm_{wt.}$. The depletion measured during each cycle was accounted for in all calculations involving hydrogen concentration, and is reflected in both solubility plots that follow. Additionally, a mass spectrometer was used to monitor the atmosphere exhaust from the test chamber, to detect any significant loss of hydrogen from the sample through desorption.

2.4. Data reduction and analysis

For hydride phase analysis, the recorded Debye–Scherrer ring patterns were integrated using Fit2D over the entire azimuthal range, rather than using partial integrations representing the transverse and rolling directions of the material. This method was chosen as it allows for the sampling of all diffracting hydride crystals, rather than those with planes aligned to diffract close to the two principle directions. This also allows for greater counting statistics to be incorporated, giving more accurate definition to low intensity peaks, along with significantly reduced background noise relative to the magnitude of the diffraction peaks of interest, thus improving the signal to noise ratio. To investigate the impact of this choice of integration, an analysis of full-width-half-maximum (FWHM) was performed on hydride peaks from a full integration (360°) and 15° azimuthally integrated data ($\psi \pm 7.5°$), taken from the two principle directions. The results showed an average of 9% peak broadening in hydride reflections from fully integrated data, which was considered acceptable.

The XY format diffractogram files generated by Fit2D were normalised against the incident beam intensity to remove synchrotron energy decay and then batch processed using the command line operator for TOPAS-Academic V5, in conjunction with an in-house developed Matlab R2014a function. In order to account for instrument broadening, peak shape parameters were defined from modelling a standard reference material and fixed throughout the analysis. As peak shape is a function of beam, detector and sample, defining this with a calibrant allows the isolation of the effect of sample on peak profile [64,65]. This then allows for any peak broadening or asymmetry to be defined using parameters related to the material being studied.

Initially the diffraction patterns were simulated using a Rietveld structural model [66,67] for accurate measurements of phase weight percentage (wt%). However, it was quickly noted that the software was not correctly emulating hydride reflections where intensities were near to extinction. Instead, an alternate method was employed, where the diffracting weight percentage of hydride from the sample in its initial condition was measured using the Rietveld method, to provide a boundary condition. This boundary condition was established as the diffracting weight fraction for the essentially-complete precipitation of $430\,ppm_{wt.}$ at T_{floor}, where the solubility of hydrogen was predicted by JMatPro to be $0.19\,ppm_{wt.}$ and was considered negligible [60]. A second boundary condition comes from the assumption that when all hydrogen was dissolved into solution, the diffracting volume was at zero and
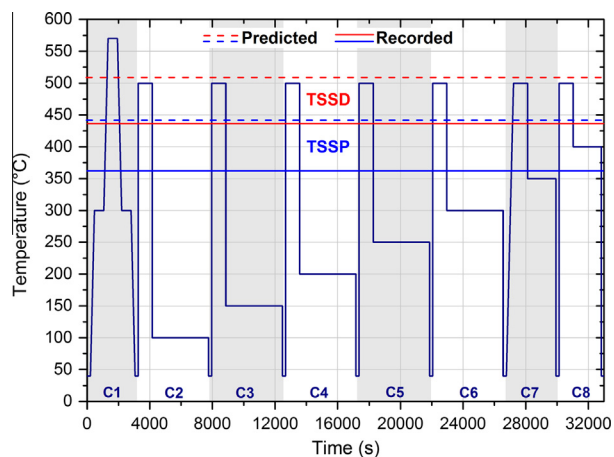

Fig. 1. Schematic of thermal operations as a function of time, with measured terminal solid solubility temperatures and those predicted by McMinn.

no peak existed. Using these two conditions, in conjunction with the assumption of a linear relationship linking volume fraction with integrated intensity, makes it possible to calculate the volume fraction of δ-hydride from the measured area of each phase within the modelled pattern [27].

Fig. 2 illustrates the diffractograms generated from fully integrated data at a number of key temperatures from throughout the experiment, over the interplanar spacing range considered. The chosen reflections for volume fraction analysis are the $\{311\}_\delta$ and $\{022\}_\delta$, with lattice spacings of ≈ 1.43 Å and ≈ 1.68 Å, respectively; decided for their high multiplicities (24 and 12) and good degree of separation from nearby matrix peaks. The 40 °C data set shows the hydride peaks at their maximum value, representing approximately 100% precipitation. Conversely, the 500 °C line shows total peak extinction where all hydrogen is in solution. The final pattern, from the end of the 300 °C isothermal hold, represents the diminished peak intensity representative of the lower volume of diffracting hydride associated with an increased solubility at this temperature.

Diffractogram modelling during batch processing was performed using the Le Bail method of the *hkl* function within TOPAS, described in detail in [68]. As with the Rietveld method, peak positions were defined by the space group and lattice parameters of the phase, while the intensities of individual reflections were allowed to vary independently of texture parameters and one another [27]. By inputting values of cell mass into the *hkl* structure of 371.616 for the hydride and 182.448 for matrix, taken from the fully refined Rietveld model, TOPAS was then able to calculate a weight percentage for each phase. Similarly to the Rietveld method, this was calculated as a function of peak area for all peaks in both phases over the given 2θ or interplanar spacing range, illustrated as the *x*-axis in Fig. 2. As the scale parameters used in each phase were allowed to refine freely to give the best possible fit to the data while accounting for the differences in peak profile between the two phases, the initial software calculated weight percentage values deviated significantly from the known boundary conditions. However, by using the aforementioned relationship it became possible to calibrate these values to show the true phase distribution for any given acquisition. In addition, JMatPro 7.0 and the ZRDATA database were used both for experimental planning and to calculate parts of the thermodynamic data underpinning the model presented.
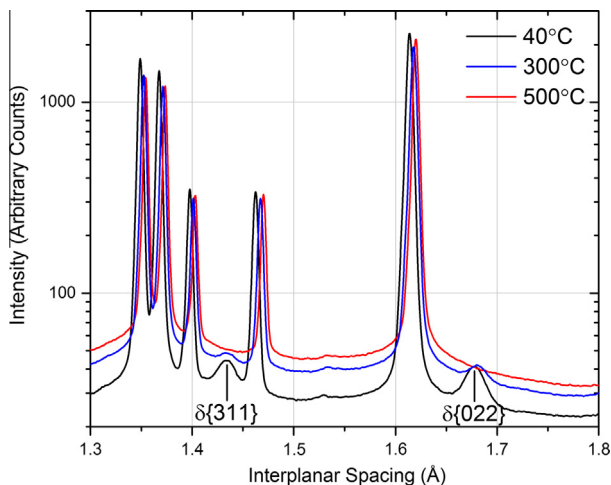
3. Results

3.1. Isothermal precipitation

From the calculated volume fraction of hydride, it becomes possible to derive the completion percentile for the precipitation process that takes place during the isothermal hold in each cycle, seen in Fig. 3. The first point on this plot, at $t = 0$, is taken as the last acquisition before the quench is performed. Given that the quench is not truly instantaneous, the second point in each series tends to lie during a period of rapid thermal change. This may artificially increase the time taken to reach completion thresholds by a small amount.

For the 100–250 °C hold cycles (C2–C5), more than 95% of hydrogen has precipitated by $t = 15$ s; recorded from the second acquisition after the quench commences. This is likely to have occurred partially during the rapid quench and partially during the first seconds of the isothermal hold. The temporal resolution derived from the method employed for diffraction pattern acquisition is insufficient to deconvolute these two effects. For the final two cycles, at temperatures greater than 250 °C, the rate of precipitation is lower and reaching maximum completion takes significantly longer than at lower temperatures. For cycle C7, a cycle that was only half the duration of others, there appears still to be some upwards slope towards the end of the data series, potentially indicating incomplete precipitation at the cessation of the cycle. Unfortunately, time constraints cut this and the precipitation-free cycle (C8) short, and so 100% completion was taken as the weight percentage value reached at the end of this dwell. This may artificially reduce the completion time for precipitation recorded at this temperature. For this reason, the final hold two hold temperatures (cycles C7 and C8) are excluded from Fig. 4.

Taking all other percentage completion data sets, it becomes possible to plot a transformation map for the precipitation process, Fig. 4. Unlike a conventional Time–Temperature–Transformation (TTT) diagram, a linear scale is used as the temporal resolution of 9–10 seconds per acquisition would make a logarithmic scale unclear in the low time region. Additionally, due to the rapid rate of precipitation that is observed, the percentage completion thresholds chosen for this analysis are limited to being close to 100%.

This map demonstrates the time taken to reach a threshold completion state in the precipitation process, as a function of the temperature at which each isothermal hold takes place. The curvature towards longer times seen in the elevated temperature region reflects the significant reduction in precipitation rate seen in later
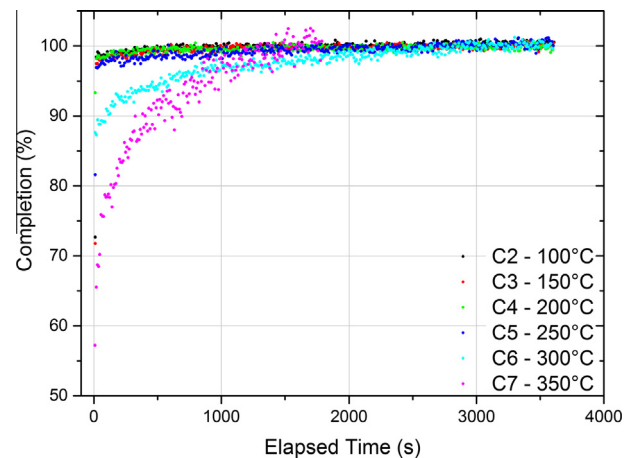

Fig. 2. Representative diffractograms from 40 °C, 300 °C and 500 °C acquisitions for the considered range of lattice spacing.

Fig. 3. Precipitation completion percentage as a function of time.

Fig. 4. Transformation map.
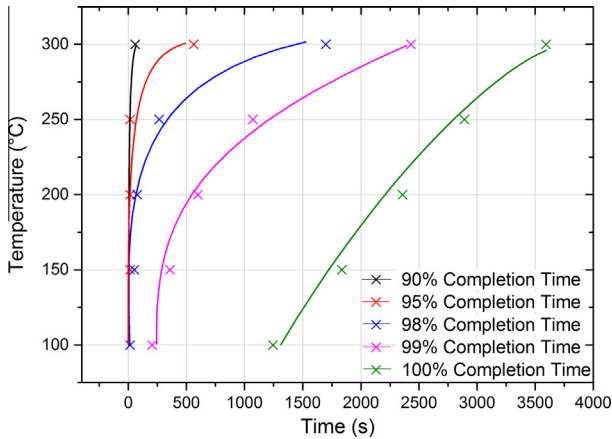

Fig. 5. Predicted and recorded hydrogen in solution curves [60].

cycles. It should be noted, however, that while the highest temperature dwells do show significantly slower precipitation than the those at lower temperatures, 90% precipitation still occurs in just 58 s during the 300 °C hold. In all series, it is clear that completion times are at their lowest at some temperature below 200 °C. For the 90–98% curves, the temporal resolution of the diffraction imaging setup acts as a limiting factor, preventing an accurate determination of the peak precipitation temperature beyond this accuracy from these curves.

In the 99% and 100% completion plots, however, curvature continues to the lowest recorded hold temperature, possibly indicating a maximum rate to precipitate hydrides close to, or lower than, the minimum experimental dwell temperature of 100 °C. It should be noted, however, that for all hold temperatures scatter in the data of between ±1% and ±3% (depending on cycle) means accurate judgement of 100% completion is difficult, and so the trend in this final series should be considered carefully.

3.2. Solubility

Values for hydrogen solubility during dissolution are calculated from the recorded weight percentage of δ-hydride during the heating ramp in cycle C1, and from the identical ramp at the beginning of the final quench cycle (C7). The diffracting weight percentage can be converted into a ppm$_{wt.}$ value, and this can subsequently be subtracted from the boundary condition of 430 ppm$_{wt.}$ to give the amount of hydrogen in solution. The dissolution solvi taken from C1 and C7 were compared as a cursory investigation into changes in solubility resulting from repeatedly cycling thermal transients. As previously mentioned, the curve measured from the final cycle showed good agreement with the initial cycle, within the bounds of expected experimental error and known depletion, indicating that the solubility is stable throughout the experimental programme.

The curve for dissolved hydrogen, determined from precipitation occurring during cycle C1, is presented in Fig. 5 alongside data for slow heating and cooling rates taken from the literature. Both the TSSP and TSSD from the literature are plotted, but the current experimental data does not show agreement with the expected TSSP from McMinn. It should be noted that the cluster of points seen at 300 °C is those recorded during a short dwell at this temperature.

The data produced by McMinn are representative of Zircaloy-2 and -4 with a number of processing states and were put forward as evidence that microstructure and chemical composition have little effect on solubility [60]. Additionally, the range of thermal transient rates used in his work, considered to be slow rates when
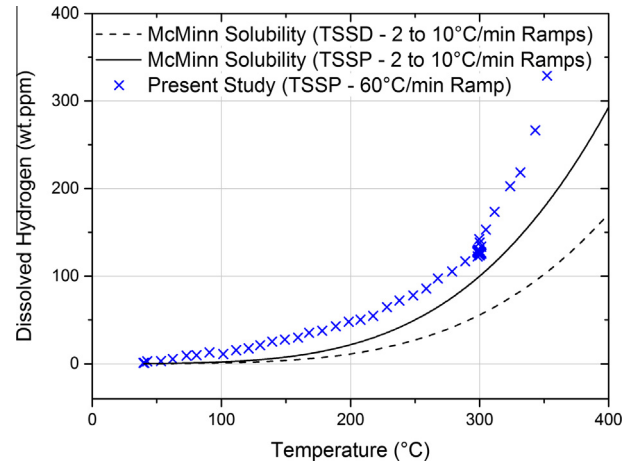
compared with the present study, were also said to have little effect on hydrogen solubility [60]. Later work, undertaken by Zanellato, put forward evidence that significantly increasing the heating or cooling rate will lower the terminal solid solubility temperature observed during each thermal operation. The greatest magnitude of shift seen in that work is of the order of 20 °C, where the cooling rate was increased by an order of magnitude from 10 °C s^{-1} to 100 °C s^{-1} [27]. Similarly, the curve for solute hydrogen concentration recorded during rapid continuous cooling in the present study shows little agreement with the slower examples published by McMinn. However, such a deviation can arise from a kinetic effect due to insufficiently fast hydride precipitation rather than a true change in solubility. To investigate this in more detail, the evolution of solute hydrogen was investigated during the series of isothermal dwells that followed C1.

Fig. 6 again shows the TSSP and TSSD curves calculated by McMinn from slow cooling studies. Also plotted are the measured quantities of hydrogen in solution at the beginning and end of each isothermal dwell region (C2–C8), as illustrated by the subplot schematic. In this figure, the black dashed and solid lines represent data from literature continuous cooling transients, while the dotted lines with cross and circle markers are those from quench and hold transients during the present study. It should be noted for clarity that no TSSD data from the present experiment is included in this figure, and that the literature TSSP has been plotted for clarity. The
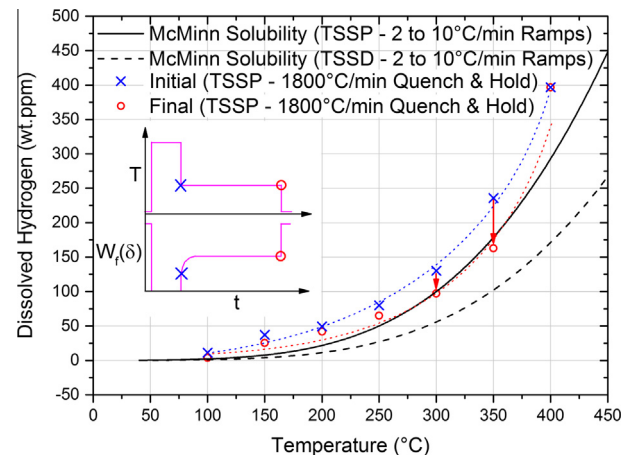

Fig. 6. Supersaturation in isothermal holds after quenching from rate limited kinetics [60].

final points in each quench series, at 400 °C, are both set at a concentration of 400 ppm$_{wt.}$, given that no precipitation was seen during that cycle and a depletion of 30 ppm$_{wt.}$ was observed by this point in the experiment.

As with the solute hydrogen measurements from continuous thermal transients, C1 and C7, the initial recorded solute hydrogen concentration during each isothermal hold has a significant positive systematic bias when compared with the literature TSSP. Instead, these points, indicated as blue crosses, show reasonable agreement with the dissolved hydrogen level recorded from continuous rapid cooling cycle, Fig. 5. When quenching at high cooling rates to elevated hold temperatures (those above 250 °C), the process of hydride precipitation continues during the hold and hydrogen leaves solution until a final concentration is recorded. The final value is well below the initial quenched solubility and that of rapid continuous cooling cycles, instead being in very close agreement with the TSSP predicted by McMinn.

Given this information, it seems possible that the TSSP curves put forward from experiments where rapid continuous cooling operations are used, do not truly represent the equilibrium solubility. In the present work, this is reflected by the process of hydride precipitation clearly being unable to occur fast enough to keep pace with the rate of temperature change. This substantiates the findings of Root, whom suggested that significant incubation times are required for the quantity of hydrogen in solution to reach true equilibrium [69].

The ramifications of this mean that proposed shifts in precipitation solubility temperature, as a function of heating/cooling rate, seen in [27] are not likely to be changes to the equilibrium solubility of the material. Instead, they may be the mark of significant supersaturation developing, as the result of the precipitation kinetics being rate limited by a reduced driving force at these temperatures. This possibility is further evidenced by the fact that in that work the dissolution solubility shifts towards lower temperatures with increasing heating rate, rather than towards higher temperatures [27]. With a high heating rate, one would expect the resulting dissolution solubility curve to either show little/no change from equilibrium or be shifted to higher temperatures, where the kinetics of the process are not fast enough to keep pace with the change of temperature. While the true equilibrium solvus temperature is defined entirely by free energy curves (and is thus free of the influence of heating and cooling rates), a shift in the apparent TSS temperature may possibly occur with high heating or cooling rates. This would be the product of a non-equilibrium microstructure being obtained at the cessation of cooling or heating.

Lastly, those values for final hydrogen in solution recorded at lower temperatures show little difference from the initial solubility points, being only a small amount above the literature TSSP line. This is because hydride precipitation is essentially complete by the first diffraction acquisition, and little or no supersaturation remains owing to the rapid kinetics at these temperatures, brought about by a high driving force for precipitation. While within expected experimental error, the positive bias at these lower temperatures (when comparing the final dissolved hydrogen concentration against the literature) may be the product of a transformation between γ- and δ-hydride, thought to occur below 260 °C [32]. While no diffraction from γ was recorded, its existence in low quantities or very fine precipitates would potentially not generate any recordable diffraction signature, and other authors have said that hydride peaks are undetectable below 20 ppm$_{wt.}$ [46]. This could then tie up hydrogen and thus reflect in an artificially increased reading of hydrogen in solution when calculated solely from δ-hydride reflections. The observation of γ-hydride tips on δ-hydrides, made by Barrow, may go some way towards justifying this possibility, as they could be in small enough volumes and quantities to minimise diffraction [25].

4. Discussion

The experimental results show that hydride precipitation kinetics become increasingly rapid with decreasing temperature over the range studied in this work. Hydrides in zirconium precipitate through a diffusion controlled process of nucleation and growth phase transformation [70,71], and in such transformations, the TTT diagram typically follows a C-shaped curve. The present results from this set of experimental data, Fig. 4, follow a profile that would correspond to the upper part of this C-shape only. In this regime, transformation kinetics are essentially limited by the thermodynamic driving force available, and as the temperature increases, the transformation is slower, as the product of a lower driving force. The lower part of a typical C-curve, which is not observed in this study, corresponds to a regime where diffusion becomes rate limiting. The present results therefore suggest that over the investigated temperature range it is the availability of sufficient driving force to overcome the significant energy barrier to hydride nucleation that dominates, and hydrogen diffusion never becomes rate limiting. This energy barrier arises from the elastic strain that is generated as a product of the misfit that forms from the large volume expansion that takes place during precipitation, as well as the energy required to form new interfaces. To explore whether this hypothesis is physically reasonable, simple classical models for nucleation and diffusion have been used to estimate the undercooling required to produce the peak nucleation rate and the diffusion distance of hydrogen. An equation that describes nucleation rate (I_v) as a function of temperature is presented as Eq. (1).

$$I_v = N_o \frac{kT}{h} \exp\left(\frac{-(G^* + Q)}{kT}\right) \tag{1}$$

Here, N_o represents the number of nucleation sites (zirconium atoms per unit volume for homogeneous nucleation), Q is the activation energy for diffusion, h and k are the Planck and Boltzmann constants, respectively, T is the temperature in Kelvin and G^* is the energy barrier for hydride nucleation, described by Eq. (2) [52].

$$G^* = \frac{9}{2} \pi \gamma_f \gamma_e^2 g_n^{-2} \tag{2}$$

This expression is comprised of three primary components, where two terms describe interfacial energy (γ_f and γ_e), and the term g_n representing nucleation energy density. As δ-hydrides are considered to take the form of a disc or oblate spheroid, two distinct surface types can be identified; the large, relatively flat surfaces possess a lower interfacial energy of $\gamma_f = 0.065 \text{J m}^{-2}$, while the edge has an interfacial energy taken to be $\gamma_e = 0.28 \text{ J m}^{-2}$ [52]. The final term in this expression can be calculated from Eq. (3) [52].

$$g_n = k_B T C_x \ln(C_s/C_{eq}) - g_\epsilon + g_{ex} \tag{3}$$

Here, k_B is Boltzmann's Constant, T is absolute temperature, C_x signifies hydrogen concentration in hydride precipitates per unit volume, calculated as a function of temperature using equilibrium values taken from JMatPro, C_s is the amount of hydrogen dissolved in the matrix and C_{eq} denotes the equilibrium solubility of hydrogen in the matrix, also from JMatPro [52]. The final two terms, g_ϵ and g_{ex} represent contributions from the strain energy associated with the volumetric misfit and that from externally applied forces, respectively [52]. As the system being considered has no externally applied load, this final term will be excluded from the model.

From Eqs. (2) and (3), there are three energies influencing the nucleation of hydrides, one acting to promote nucleation and precipitation, and two acting to hinder it. The chemical free energy that drives precipitation is described by the term $k_B T C_x \ln(C_s/C_{eq})$ in Eq. (3), and arises from an excess of hydrogen in solution over

the equilibrium concentration. The two converse terms are those of the energy required to form new interfaces during nucleation and precipitation, described in Eq. (2), and the energy required to form a precipitate that misfits with the encompassing matrix and must generate strain to exist.

Eq. (4) calculates the strain energy of any shape of precipitate, given uniform dilatation, through the Eshelby approach, while assuming no plastic relaxation takes place [72]. This technique describes a precipitate with an associated isotropic misfit and isotropic elastic properties, within an infinite and elastically isotropic parent matrix, and simulates equal deformation in both the parent and precipitate [50].

$$g_\epsilon = \frac{2}{9} \cdot \frac{(1+v)}{(1-v)} \mu (\Delta^T)^2 v^\beta \qquad (4)$$

In this expression, v is Poisson's ratio, μ is the shear modulus for the parent matrix, Δ^T is the cubic dilatation in an unconstrained transformation, and v^β is the specific atomic volume of the precipitate phase [72]. For the purpose of this work, the expression derived by Sing et al. for volumetric expansion as a function of absolute temperature will be used, where $\Delta^T = 0.1506 + 7.38 \times 10^{-5} T$ [45]. When utilising the Eshelby method to calculate strain energy, it is then assumed that this overall volume expansion is split evenly between all directions, rather than occurring anisotropically. The value for v^β in this expression is taken as the volume of a stable nucleus, calculated for an oblate spheroid morphology with the two major axes being equal to the critical radius (r^*), derived for each temperature considered within the model. It should be noted that from the work of Barrow et al., elastic strains in the matrix are up to $4\times$ greater than those seen in the hydride, and as the Eshelby model considers uniform deformation in both, values predicted through this method are an approximation rather than being absolute.

In previous attempts to model the hydride precipitation, a single temperature independent value of 1×10^8 J m^{-3} for strain energy has been used [52]. Accounting for the temperature dependence of the misfit, the values produced by the Eshelby model range from 1.21×10^7 J m^{-3} at 0 °C to 5.79×10^9 J m^{-3} at 500 °C. When compared with the isothermal value given by Massih et al., this would correspond to a temperature of approximately 265 °C in the present system. From the work of Puls, and later used by Barrow et al., a value of 1.66×10^7 J m^{-3} is calculated, which corresponds to the strain energy calculated through the Eshelby method at 50 °C [46,73]. The present results suggest that if the misfit varies as reported in [45], then the range of misfit strains with temperature is large and cannot be ignored in attempts to simulate hydride precipitation. In reality the situation is further complicated because plastic relaxation may take place, and the degree of which will also be temperature dependent, where softening will occur at elevated temperatures. Nevertheless, in the nucleation stage, it is expected that the larger misfit at elevated temperature exacerbates the effect of decreased chemical driving force, further slowing the nucleation kinetics.

Fig. 7 contains the result of the nucleation model for three considered scenarios; with no strain energy contribution, where the rate and peak temperature are highest, and including strain energy, derived from the Eshelby model, for both a disc and an oblate spheroid precipitate. From this, it can be seen that the peak nucleation rate is predicted between 113 °C and 149 °C, depending on the chosen system, which is reasonably consistent with the transformation map, Fig. 4. Strain energy is shown to have a significant effect on both the magnitude and position of the nucleation rate peak, reducing the optimum temperature for nucleation by 17 °C and 36 °C for an oblate spheroid and disc morphology, respectively. However, the main factor that is responsible for the high degree of
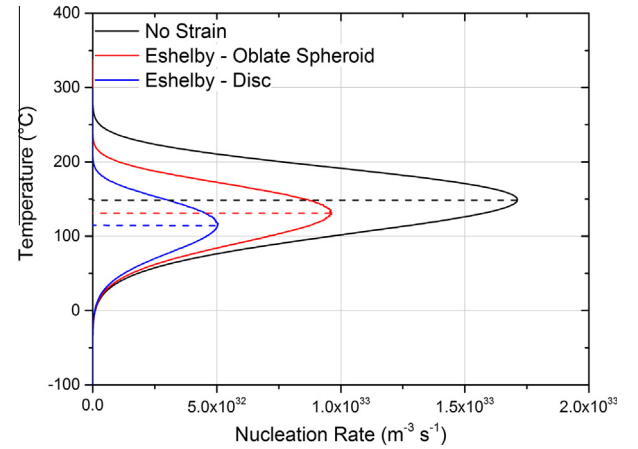

Fig. 7. Calculated nucleation rate as a function of temperature, strain energy and geometry.

undercooling required to reach the peak nucleation rate is the relatively high interfacial energy reported for the hydride phase, an observation also made in previous studies [46]. Below the peak nucleation temperature, the process of hydrogen diffusion becomes the controlling influence within the model, where the local jumping of hydrogen over the interface regulates the rate of the process. It is noted that at high temperatures (300 °C and greater), where experiments show continued precipitation, this figure suggests a nucleation rate close to zero. This is untrue, as substantial nucleation is still predicted by the model at these elevated temperatures in the strain-free system (of the order of 10^{27} m^{-3} s^{-1} at 300 °C, for example), although the introduction of strain energy does reduce this considerably.

Clearly, the present model is very simple, and in practice, nucleation of hydrides is heterogeneous, rather than homogeneous. However, heterogeneous nucleation of hydrides at features such as dislocations or sympathetically in the strain field created by other hydrides would serve only to reduce the strain energy component of the nucleation energy barrier. As Fig. 7 shows, even if there is no strain energy required (through complete, instantaneous relaxation), a large undercooling for nucleation is still required, owing to the interfacial energy terms.

To understand why the lower portion of the expected C-curve was not observed, even at precipitation temperatures as low as 100 °C, simple diffusion distance calculations have been performed for hydrogen dissolved in zirconium. Taking the diffusion coefficient determined by Kammenzind et al. for hydrogen in Zircaloy-4 (288–482 °C), and extrapolating to cover a range relevant to the present work, it becomes possible to estimate the diffusion length for hydrogen [74]. This is done using a simple $d = \sqrt{Dt}$ approximation, where D is the diffusion coefficient and t is time.

Fig. 8 shows the result of these diffusion distance calculations at two length scales, where (a) is scaled to half the axial length of the test piece, giving an indication of how far from the centre of the sample, where diffraction measurements are taken, hydrogen is able to diffuse. Both subplots consider diffusion to be isotropic for simplicity, however, given the highly textured nature of zirconium cladding this may not be true of all directions within a component. The data contained in (a) serve to illustrate that with elevated temperatures and long hold times, hydrogen is able to diffuse moderate distances through the zirconium matrix. Given an hour at 500 °C, the diffusion distance is calculated as 1.2 mm, which is 12% of the distance from the point of beam incidence to the ETMT grips, demonstrating why axial hydrogen distribution checks are important.
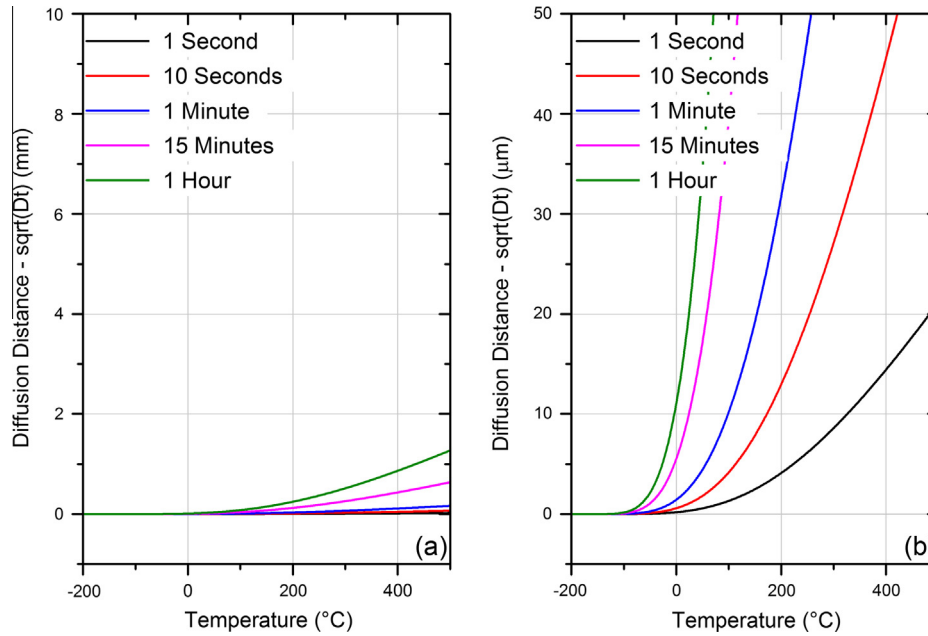
Fig. 8. Diffusion distance as a function of temperature, showing distances relevant to (a) axial sample length and (b) inter-hydride spacing.

Fig. 8 – (b) looks specifically at distances relevant to both the inter-hydride spacing and overall precipitate length related to the sample being studied. The average zirconium grain diameter for the sample measures 10 µm, micro-hydride lengths typically range from 10 nm to 200 nm (although examples of large 1 µm precipitates exist) and the inter-hydride spacing taken from transmission electron micrographs is no more than 2 µm. These values were recorded for the specific sample being examined in this work, and as hydride geometry and distribution will change with hydrogen concentration, thermal history and mechanical processing, this assessment is intended to be representative, rather than definitive. Taking the curve for 1 s, it is evident that hydrogen is capable of rapidly diffusing the average measured inter-hydride spacing at temperatures close to 150 °C. Similarly, it is also able to diffuse half of the width of a matrix grain in just ten seconds at this temperature.

The overall rate of transformation is limited either by the energy barrier or diffusion rate at upper and lower temperatures, respectively, giving the customary C-shaped curve to TTT diagrams. The values for local diffusion distances above would suggest that while the diffusion of hydrogen controls the process of precipitation at temperatures below 0 °C, the presence of rapid diffusion at temperatures relevant to fuel assemblies would mean that diffusion is never rate limiting. This explains the extremely fast precipitation observed below 150 °C, where 98% of precipitation is complete almost immediately. As temperatures increase above 150 °C, the drop in precipitation rate observed in Fig. 4 then occurs through the activation energy becoming the rate limiting process. It should be noted, however, that while hydrogen diffusion is considered not to be rate limiting above 0 °C the process of nucleation is still dependent on short range diffusion, where the local jumping of hydrogen across the interface regulates the speed of nucleation.

Where hydrogen concentrations are significantly lower, such as in the case of CANDU pressure tubes where the life design allowance is 100 ppm$_{wt.}$ of hydrogen, the inter-hydride spacing would in-turn be larger [75]. Such increases in the required distance for hydrogen to travel could then lead to diffusion becoming a rate-limiting factor. From the diffusion data above this would seemingly not be until inter-hydride spacing was in the order of tens of microns, at least. For the purpose of this work, however, the above assessment of diffusion distance seems sufficient to explain the lack of the lower half of the C curve expected in a conventional TTT diagram.

5. Conclusion

Synchrotron X-ray diffraction was able to investigate successfully the isothermal precipitation of hydrides within Zircaloy-4. From completion percentage data, a peak in precipitation rate was measured close to, or below, 100 °C. The measured concentration of hydrogen in solution while precipitating, recorded during a 1 °C s^{-1} cooling transient, was shown to be in poor agreement with the literature. During quench and hold cycles, the initial solubility showed a similar agreement with the continuous cooling values, but then continued to drift towards the position of the literature solubility. This was explained as being the product of significant residual supersaturation, where the process of precipitation was unable to keep pace with the rate of temperature change. This effect was primarily seen at temperatures above 200 °C, while those below this threshold showed little or no recordable residual supersaturation after the quench, within the bounds of experimental error.

A simple model was used to predict the peak temperature for hydride nucleation using the Eshelby method for estimating misfit strain energy in two geometries of precipitate, as well as performing a strain energy-free calculation. This represents a lower and upper bound to nucleation rate behaviour, respectively. The temperature dependence of the misfit was included in this model and shown to be significant in the calculation of strain energy. While only a simple approximation, this model is reasonably consistent with the experimental observations, predicting a peak in nucleation rate at between 113 °C and 149 °C. Strain energy has a modest effect, reducing the temperature of peak nucleation rate by up to 36 °C, depending on the precipitate geometry considered. The reason a large undercooling is required to reach the peak nucleation rate is mainly attributed to the relatively high interfacial energy reported in the literature for the hydrides. Diffusion

distance calculations showed that hydrogen diffusion was not significantly rate limiting given the diffusion distances required at temperatures relevant to the life of zirconium clad fuel assemblies.

Ultimately, these simulations act to justify the experimental observations made through synchrotron X-ray diffraction. However, it should be noted that while precipitation at these higher temperatures is considered relatively slow when compared with the lower thermal region, the overall process of hydride precipitation in zirconium alloys is very rapid, owing to the high mobility of hydrogen and the large driving force that develops with increased undercooling.

Acknowledgements

References

[1] D.O. Northwood, Mater. Des. 6 (1985) 58.
[2] A.V. Nero, Am. J. Phys. 48 (1980) 327.
[3] R.A. Knief, Nuclear Engineering: Theory and Technology Of Commercial Nuclear Power, American Nuclear Society, La Grange Park, Illinois, 1992.
[4] E.C. Miller, in: Zircon. Zircon. Alloy, American Society for Metals, Cleveland, Ohio, 1953.
[5] P.E. MacDonald, T.R. Mager, M. Brumovsky, M. Erve, M.J. Banic, C. Fardy, P. Tipping, J. Pachner, Assessment and Management of Ageing of Major Nuclear Power Plant Components Important to Safety: PWR Pressure Vessels, International Atomic Energy Agency, Vienna, Austria, 1999.
[6] A. Durmayaz, H. Yavuz, Appl. Energy 69 (2001) 39.
[7] F. Garzarolli, H. Stehle, E. Steinberg, in: Zircon. Nucl. Ind. Elev. Int. Symp., American Society for Testing and Materials, 1996.
[8] M. Yamamoto, S. Naito, M. Mabuchi, T. Hashino, J. Phys. Chem. 93 (1989) 5203.
[9] M. Yamamoto, S. Naito, M. Mabuchi, T. Hashino, J. Phys. Chem. 96 (1992) 3409.
[10] B. Cox, J. Alloys Compd. 256 (1997) 244.
[11] J.P. Abriata, J. Garcés, R. Versaci, Bull. Alloy Phase Diagrams 7 (1986) 116.
[12] H. Okamoto, J. Phase Equilibria Diffus. 27 (2006) 548.
[13] B. Cox, P. Rudling, IZNA-1 SPECIAL TOPICS REPORT: Hydriding Mechanisms and Impact on Fuel Performance, Surahammar, Sweden, 2004.
[14] J. Wei, Effect of Hydrogen on the Corrosion Performance of Zirconium Alloys, The University of Manchester, 2012.
[15] G.J.C. Carpenter, J. Nucl. Mater. 48 (1973) 264.
[16] G.J.C. Carpenter, J.F. Watters, J. Nucl. Mater. 73 (1978) 190.
[17] C.J. Simpson, C.E. Ells, J. Nucl. Mater. 52 (1974) 289.
[18] S.R. MacEwen, C.E. Coleman, C.E. Ells, J. Faber jr, Acta Metall. 33 (1985) 753.
[19] D.J. Cameron, R.G. Duncan, J. Nucl. Mater. 68 (1977) 340.
[20] J.J. Kearns, J. Nucl. Mater. 22 (1967) 292.
[21] C.E. Ells, J. Nucl. Mater. 28 (1968) 129.
[22] A. Steuwer, J.R. Santisteban, M. Preuss, M.J. Peel, T. Buslaps, M. Harada, Acta Mater. 57 (2009) 145.
[23] E. Tulk, M. Kerr, M.R. Daymond, J. Nucl. Mater. 425 (2012) 93.
[24] K.B. Colas, A.T. Motta, M.R. Daymond, M. Kerr, J.D. Almer, P. Barberis, S.W. Dean, J. ASTM Int. 8 (2011) 103033.
[25] A.T.W. Barrow, A. Korinek, M.R. Daymond, J. Nucl. Mater. 432 (2013) 366.
[26] J.S. Bradbrook, G.W. Lorimer, N. Ridley, J. Nucl. Mater. 42 (1972) 142.
[27] O. Zanellato, M. Preuss, J.-Y. Buffiere, F. Ribeiro, A. Steuwer, J. Desquines, J. Andrieux, B. Krebs, J. Nucl. Mater. 420 (2012) 537.
[28] N.A.P. Kiran Kumar, J.A. Szpunar, Mater. Sci. Eng. A 528 (2011) 6366.
[29] B. Cox, J. Alloys Compd. 256 (1997) L4.
[30] N.A.P. Kiran Kumar, J.A. Szpunar, Z. He, J. Nucl. Mater. 403 (2010) 101.
[31] K.B. Colas, A.T. Motta, J.D. Almer, M.R. Daymond, M. Kerr, A.D. Banchik, P. Vizcaino, J.R. Santisteban, Acta Mater. 58 (2010) 6575.
[32] K. Une, S. Ishimoto, J. Nucl. Mater. 322 (2003) 66.
[33] R.N. Singh, P. Stahle, K. Sairam, M. Ristmana, S. Banerjee, in: Int. Work. Hydrog. Embrittlement Met., Bhabha Atomic Research Centre, Mumbai, 2008, pp. 160–170.
[34] X.Q. Ma, S.Q. Shi, C.H. Woo, L.Q. Chen, Mater. Sci. Eng. A 334 (2002) 6.
[35] S.C. Lin, M. Hamasaki, Y.D. Chuang, Y.M. Hamasaki, D. Chuang, J. Nucl. Sci. Eng. 71 (1979) 251.
[36] W. Yeniscavich, R.A. Wolfe, R.M. Lieberman, J. Nucl. Mater. 1 (1959) 271.
[37] C.L. Whitmarsh, Review of Zircaloy-2 and Zircaloy-4 Properties Relevant to N.S. Savannah Reactor Design, Oak Ridge, Tennessee, 1962.
[38] S. Arsene, J.B. Bai, P. Bompard, Metall. Mater. Trans. A 34 (2003) 553.
[39] V. Grigoriev, B. Josefsson, B. Rosborg, in: Zircon. Nucl. Ind. Elev. Int. Symp., American Society for Testing and Materials, 1996.
[40] P.H. Kreyns, W.F. Bourgeois, P.L. Charpentier, B.F. Kammenzind, D.G. Franklin, C.J. White, in: Zircon. Nucl. Ind. Elev. Int. Symp., American Society for Testing and Materials, 1996.
[41] I.G. Ritchie, C.E. Coleman, M. Roth, V. Grigoriev, Delayed Hydride Cracking in Zirconium Alloys in Pressure Tube Nuclear Reactors, International Atomic Energy Agency, Vienna, Austria, 2004.
[42] P. Efsing, K. Pettersson, in: Zircon. Nucl. Ind. Twelfth Int. Symp., American Society for Testing and Materials, West Conshohocken, PA, 2000.
[43] X.H. Guo, S.Q. Shi, Q.M. Zhang, X.Q. Ma, J. Nucl. Mater. 378 (2008) 110.
[44] J.R. Santisteban, M.A. Vicente-Alvarez, P. Vizcaíno, A.D. Banchik, J.D. Almer, Acta Mater. 58 (2010) 6609.
[45] R.N. Singh, P. Ståhle, A.R. Massih, A.A. Shmakov, J. Alloys Compd. 436 (2007) 150.
[46] A.T.W. Barrow, C. Toffolon-Masclet, J. Almer, M.R. Daymond, J. Nucl. Mater. 441 (2013) 395.
[47] X.H. Guo, S.Q. Shi, Q.M. Zhang, X.Q. Ma, J. Nucl. Mater. 378 (2008) 120.
[48] S.-Q. Shi, Z. Xiao, J. Nucl. Mater. 459 (2015) 323.
[49] L. Thuinet, A. Legris, L. Zhang, A. Ambard, J. Nucl. Mater. 438 (2013) 32.
[50] J.D. Eshelby, Eng. Sci. 241 (1957) 376.
[51] J.D. Eshelby, Eng. Sci. 252 (1959) 561.
[52] A.R. Massih, L.O. Jernkvist, Comput. Mater. Sci. 46 (2009) 1091.
[53] J.A. Gruber, S.A. Brown, G.A. Lucadamo, J. Nucl. Mater. 408 (2011) 176.
[54] J. Rashid, B. Dunham, Y. Zhang, R. Montgomery, Spent Fuel Transportation Applications: Longitudinal Tearing Resulting from Transportation Accidents – A Probabilistic Treatment, Palo Alto, CA, 2006.
[55] H. Weidinger, in: 6. Int. Conf. WWER Fuel Performance, Model. Exp. Support, Albena, Bulgaria, 2006, pp. 20.
[56] T. Tschentscher, P. Suortti, J. Synchrotron Radiat. 5 (1998) 286.
[57] P. Suortti, T. Buslaps, P. Fajardo, V. Honkimäki, M. Kretzschmer, U. Lienert, J.E. McCarthy, M. Renier, A. Shukla, T. Tschentscher, T. Meinander, J. Synchrotron Radiat. 6 (1999) 69.
[58] M. Andreas, Effect of Different Loading Conditions on the Accumulation of Residual Strain in a Creep Resistant 1% CrMoV Steel – A Neutron and X-Ray Diffraction Study PAR, École Polytechnique Fédérale de Lausanne, 2013.
[59] K.B. Colas, Kinetics of Zirconium Hydride Precipitation and Reorientation Studied Using Synchrotron Radiation, Pennsylvania State University, 2009.
[60] A. McMinn, E.C. Darby, J.S. Schofield, in: P. Sabol, G.D. Moan (Eds.), Zircon. Nucl. Ind. Twelfth Int. Symp., American Society for Testing and Materials, West Conshohocken, PA, 2000, pp. 173–195.
[61] J.H. Root, W.M. Small, D. Khatamian, O.T. Woo, Acta Mater. 51 (2003) 2041.
[62] H.S. Hong, S.J. Kim, K.S. Lee, J. Nucl. Mater. 257 (1998) 15.
[63] A. Sawatzky, J. Nucl. Mater. 2 (1960) 321.
[64] D. Balzar, N. Audebrand, M.R. Daymond, A. Fitch, A. Hewat, J.I. Langford, A. Le Bail, D. Louër, O. Masson, C.N. McCowan, N.C. Popa, P.W. Stephens, B.H. Toby, J. Appl. Crystallogr. 37 (2004) 911.
[65] R.W. Cheary, A.A. Coelho, J.P. Cline, J. Res. Inst. Stand. Technol. 109 (2004) 1.
[66] L.B. McCusker, R.B. Von Dreele, D.E. Cox, D. Louër, P. Scardi, J. Appl. Crystallogr. 32 (1999) 36.
[67] H.M. Rietveld, J. Appl. Crystallogr. 2 (1969) 65.
[68] A. Le Bail, Powder Diffr. 20 (2005) 316.
[69] J.H. Root, R.W.L. Fong, J. Nucl. Mater. 232 (1996) 75.
[70] Z. Zhao, J.-P. Blat-Yrieix, J.-P. Morniroli, A. Legris, L. Thuinet, Y. Kihn, A. Ambard, L. Legras, M. Limback, B. Kammenzind, S.W. Dean, J. ASTM Int. 5 (2008) 101161.
[71] V. Tikare, P.D. Weck, M.V Glazoff, Model for Simulation of Hydride Precipitation in Zr-Based Used Fuel Claddings: A Status Report on Current Model Capabilities, 2013.
[72] J.W. Christian, The Theory of Transformations in Metals and Alloys, first ed., Pergamon Press, London, 1965.
[73] M.P. Puls, Hydrogen Induced Delated Cracking: 2. Effect of Stress on Nucleation, Growth and Coarsening of Zirconium Hydride Precipitates, Pinawa, 1984.
[74] B.F. Kammenzind, D.G. Franklin, H.R. Peters, W.J. Duffin, Hydrogen Pickup and Redistribution In Alpha-Annealed Zircaloy-4, West Mifflin, PA, 1996.
[75] Record of Proceedings, Including Reasons for Decision: Application to Renew the Power Reactor Operating Licence for the Pickering Nuclear Generating Station, Canadian Nuclear Safety Commission, 2013.